Supplementary Material

Trace Mn decorating nitrogen-doped carbon electrocatalysts for self-powered Bio-electro-Fenton cell toward simulated wastewater treatment

Jun Xiao[a], Fengfeng Xiong[a], Shenjie Yu[a], Kai Chen[b], Suqin Ci[a*], Zhenhai Wen[a, b*]

a Key Laboratory of Jiangxi Province for Persistent Pollutants Control, National-Local Joint Engineering Research Center of Heavy Metals Pollutants Control and Resource Utilization and Resources Recycle, Nanchang Hangkong University, Nanchang 330063, Jiangxi, China

b CAS Key Laboratory of Design and Assembly of Functional Nanostructures, and Fujian Provincial Key Laboratory of Materials and Techniques toward Hydrogen Energy, Fu jian Institute of Research on the Structure of Matter, Chinese Academy of Sciences, Fuzhou, Fujia n, 350002, China.

** Corresponding authors*

E-mail: sqci@nchu.edu.cn, wen@fjirsm.ac.cn

1. Experimental section

1.1. Materials

Tris(hydroxymethyl) aminomethane (99%), Dopamine hydrochloride (98%), $Mn(NO_3)_2 \cdot 4H_2O$ (＞98%), $FeCl_2 \cdot 4H_2O$ (AR), Multi-walled carbon nanotubes (>98wt%), KOH (90%), HCl (35-37%), HNO_3 (60%), Rhodamine B, Anhydrous ethanol (94.5%), Nafion solution (5 wt%), DI water.

1.2. Characterization

The surface morphology of the samples was examined using a SU-8010 scanning electron microscope (SEM) and a Talos F200X transmission electron microscope (TEM) from ZEISS. X-ray diffraction (XRD) patterns were obtained using a Model D8 Avance X-ray diffractometer (Bruker, Germany) with Cu Kα radiation. X-ray photoelectron spectroscopy (XPS) measurements were performed using an ESCALAB 250Xi XPS spectrometer (Thermo Scientific) with Al Kα as the excitation source, and the data and peak fitting were analyzed using Casa XPS software. Raman spectroscopy was conducted using a DXR spectroscopy system (Thermo Scientific) with a 532 nm Ar ion laser to analyze the molecular structure. The metal content in catalyst was measured by inductively coupled plasma (ICP).

2. Figures

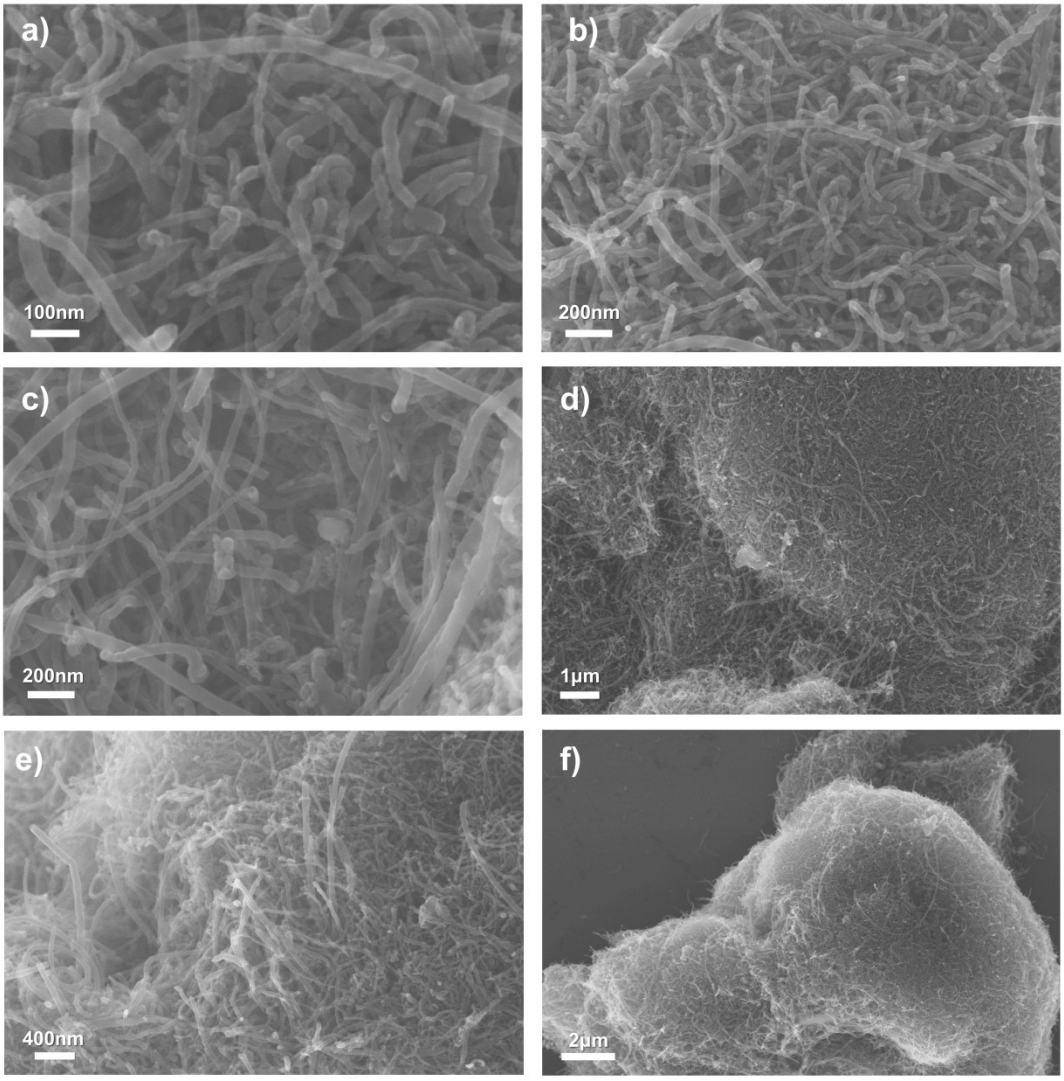

Figure S1 SEM image of a-b) PDA/CNTs, c-d) Mn-PDA/CNTs-1, e-f) Mn-PDA/CNTs-3.

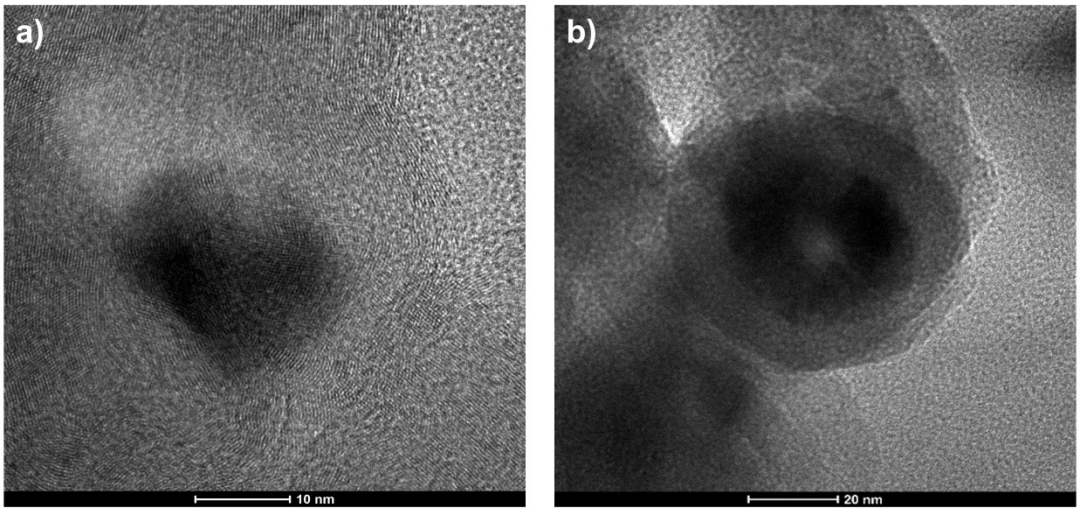

Figure S2 TEM image of the Mn-PDA/CNTs-2.

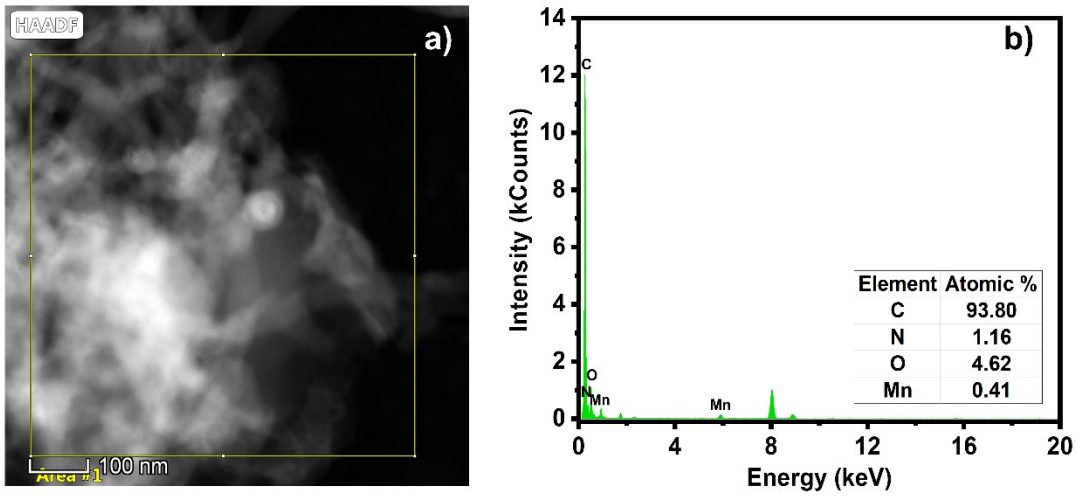

Figure S3 Energy Dispersive spectrometer (EDS) spectra for the Mn-PDA/CNTs-2 of the yellow box region in Figure a (inset: Atomic percentage of EDS elements).

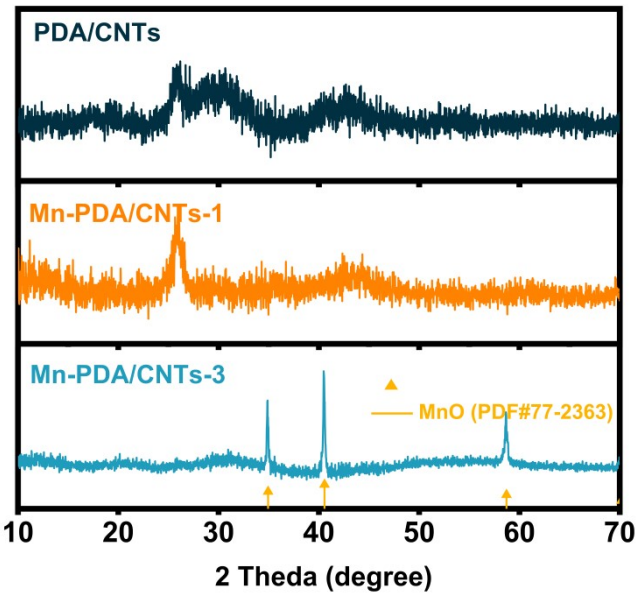

Figure S4 XRD of PDA/CNTs, Mn-PDA/CNTs-1 and Mn-PDA/CNTs-3.

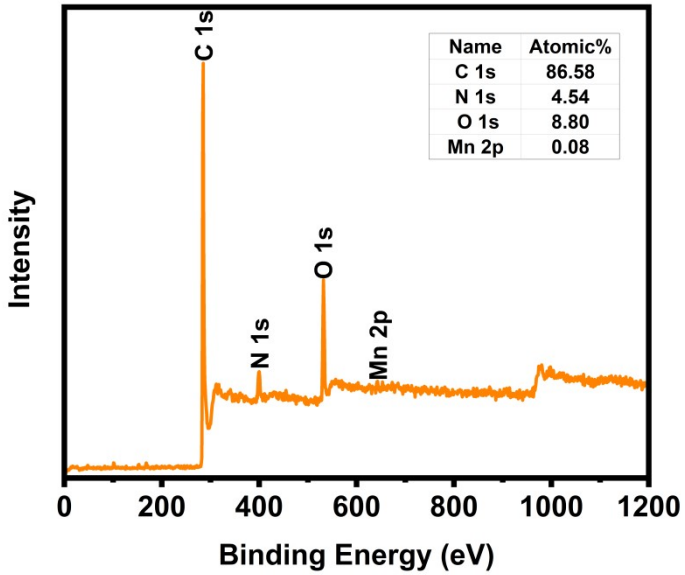

Figure S5 XPS spectra of the Mn-PDA/CNTs-2 (inset: XPS elemental analysis).

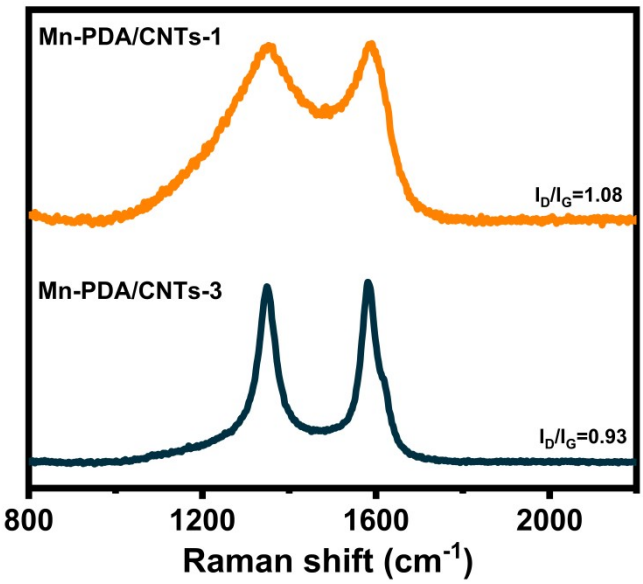

Figure S6 Raman spectrum of of PDA/CNTs, Mn-PDA/CNTs-1 and Mn-PDA/CNTs-2 and Mn-PDA/CNTs-3.

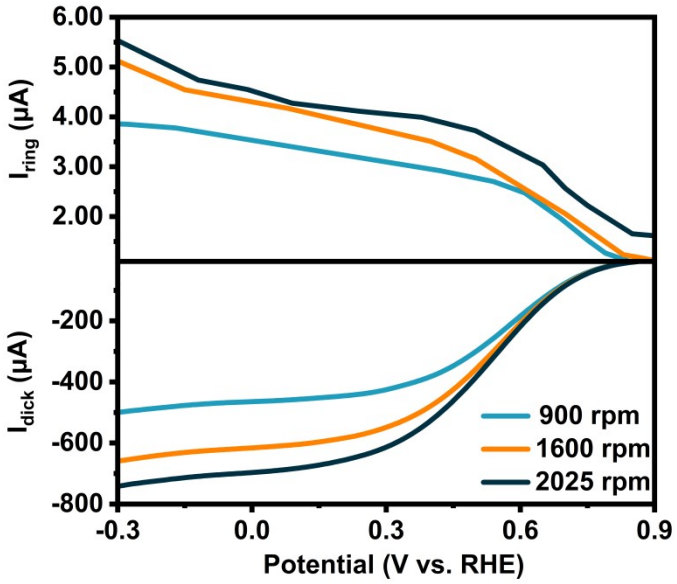

Figure S7 RRDE test diagrams at different rotational speeds.

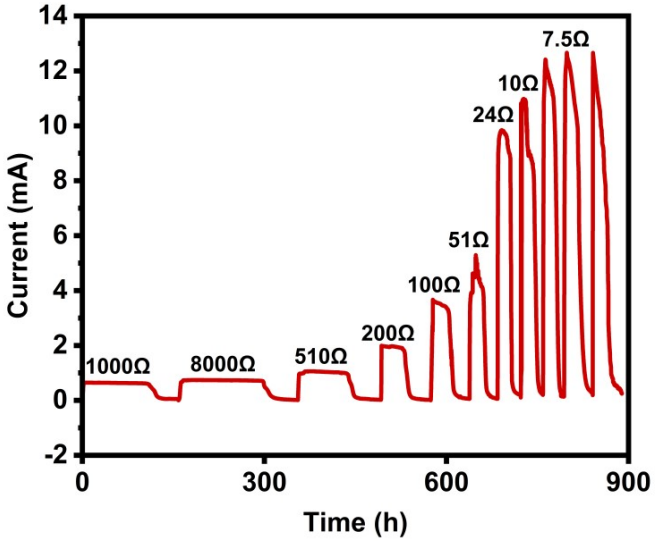

Figure S8 Domestication current changes in MFCs.

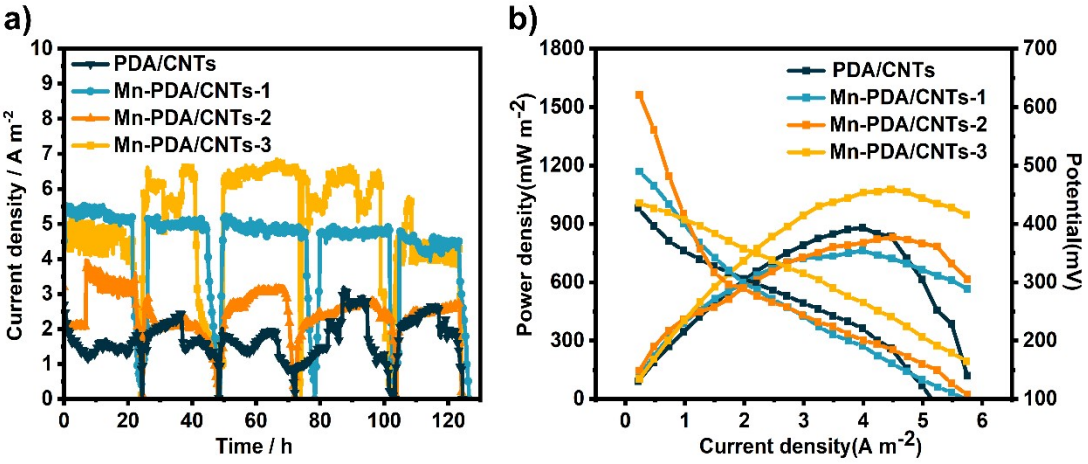

Figure S9 CCE for MFCs cathode using different catalysts preparation a) Current density diagram. b) The power density and polarization curve.

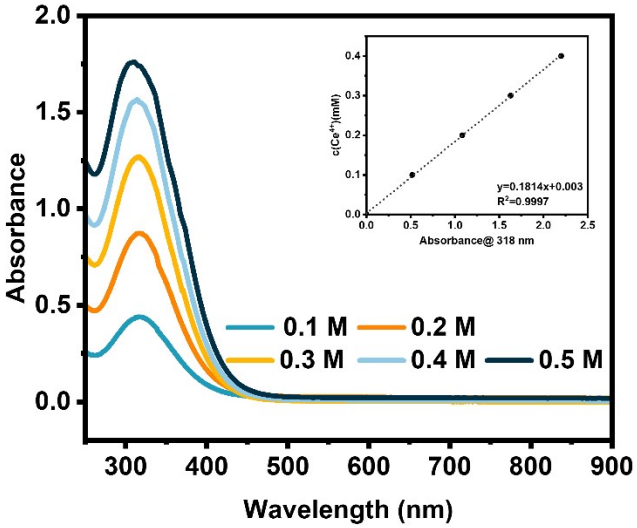

Figure S10 Absorption spectra of standard solutions of 0.5 mM $Ce(SO_4)_2$ (dissolved in 0.5 M H_2SO_4) (inset: the resultant calibration curve at the peak wavelength of 318 nm).

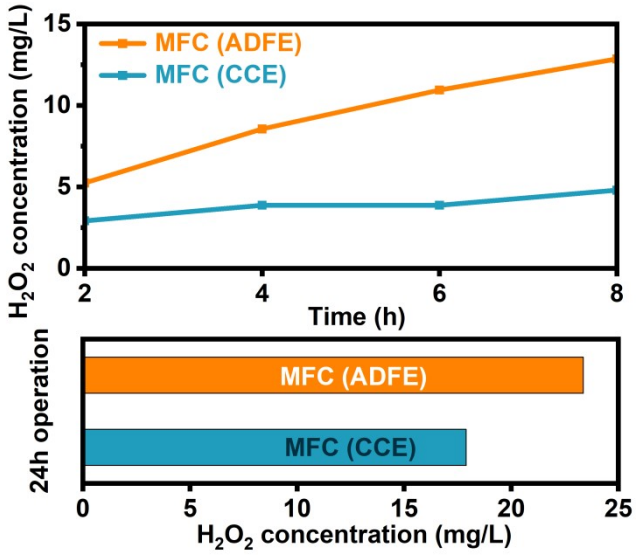

Figure S11 The cumulative concentration of H_2O_2 generated by the CCE and ADFE as the cathode.

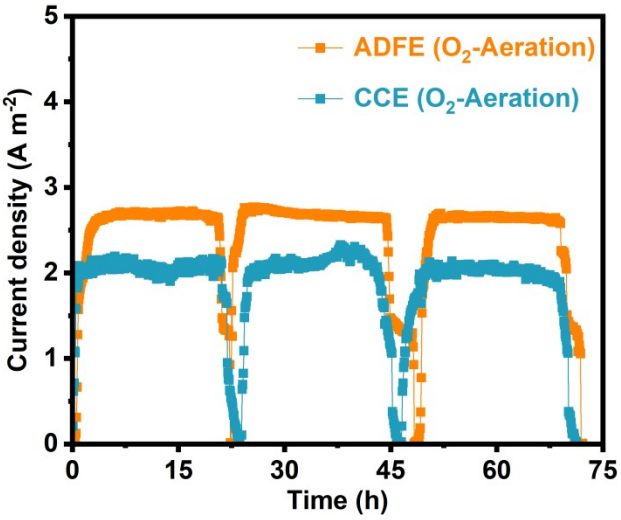

Figure S12 Current density diagram at different electrodes in MFCs.

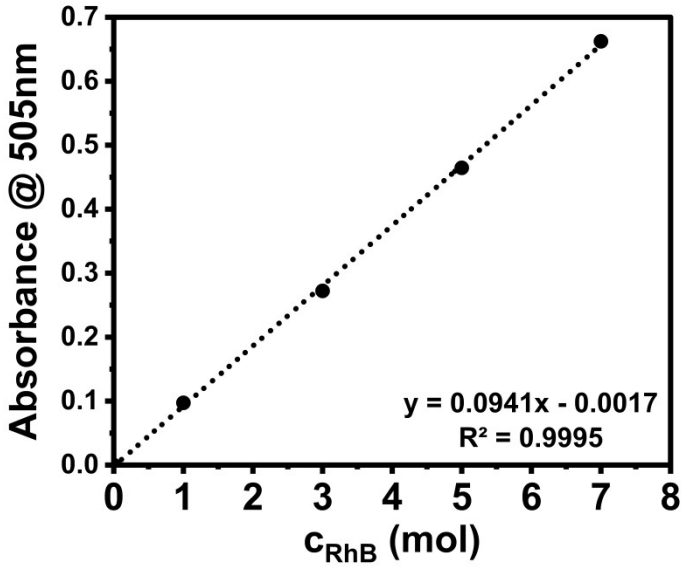

Figure S13 The resultant calibration curve of RhB at the peak wavelength of 505 nm.

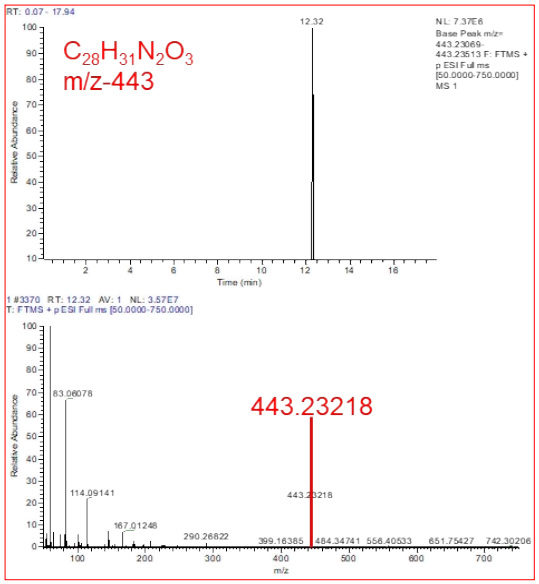
$C_{28}H_{31}N_2O_3$
m/z-443
443.23218

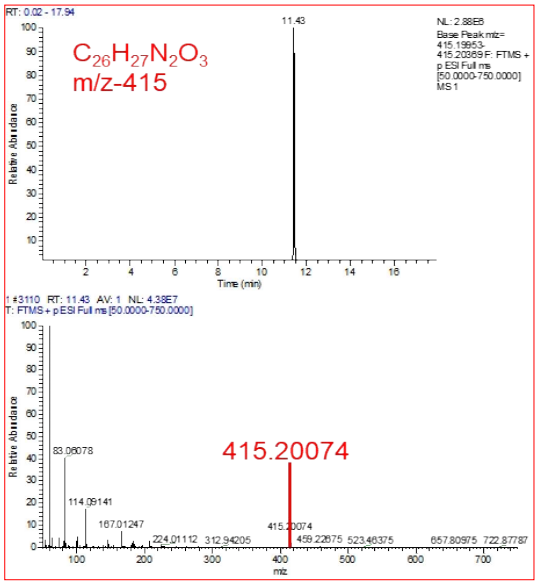
$C_{26}H_{27}N_2O_3$
m/z-415
415.20074

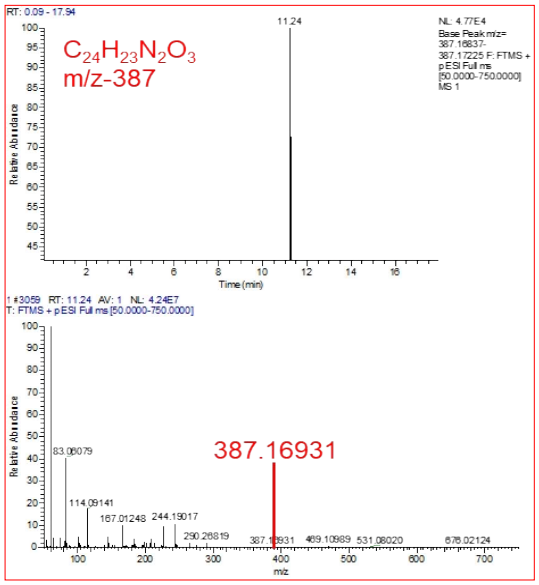
$C_{24}H_{23}N_2O_3$
m/z-387
387.16931

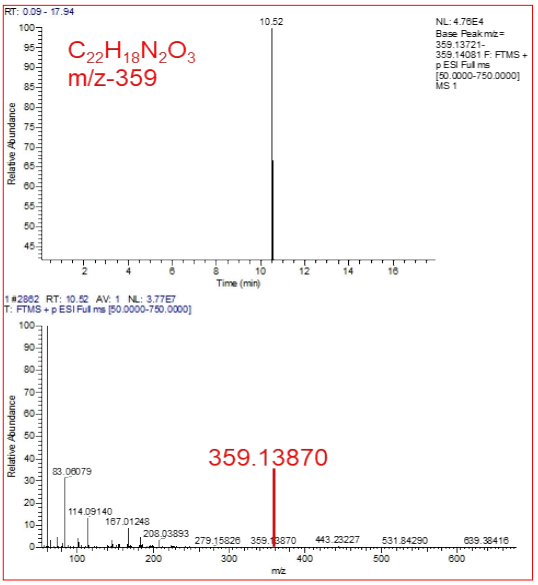
$C_{22}H_{18}N_2O_3$
m/z-359
359.13870

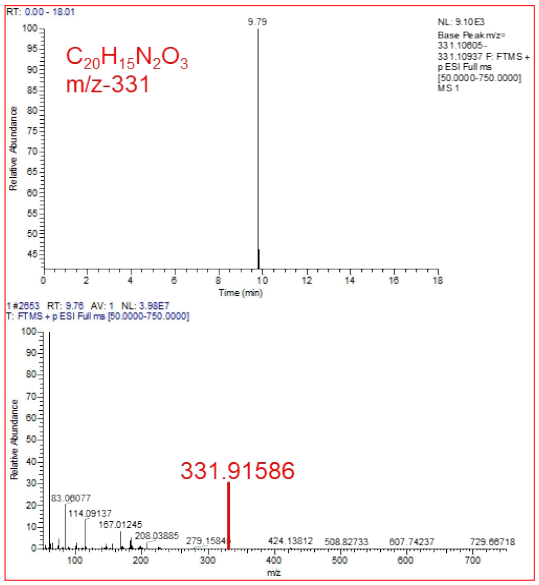
$C_{20}H_{15}N_2O_3$
m/z-331
331.91586

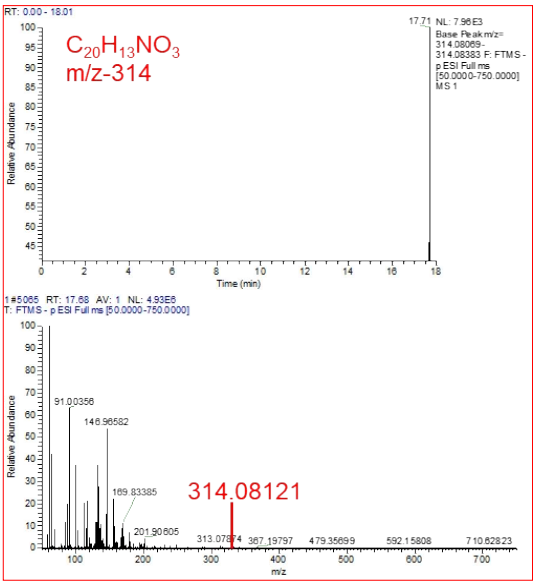
$C_{20}H_{13}NO_3$
m/z-314
314.08121

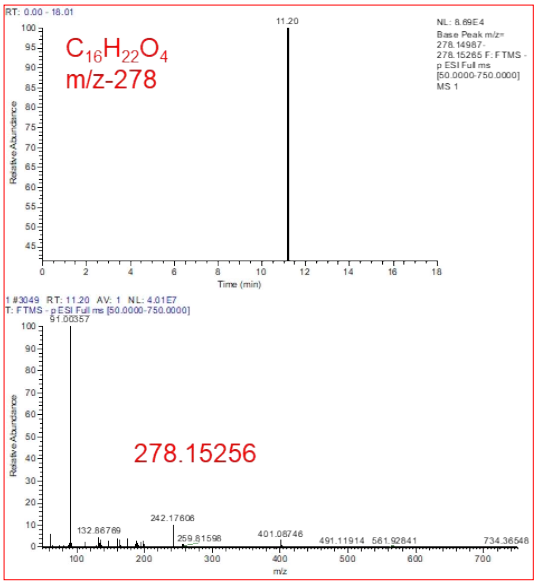
$C_{16}H_{22}O_4$
m/z-278
278.15256

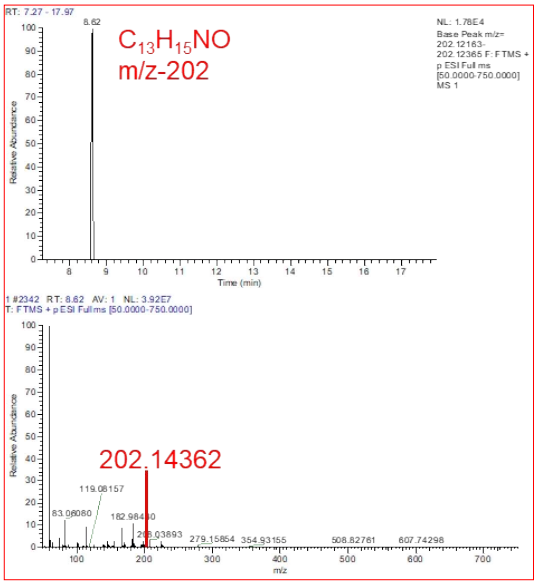
$C_{13}H_{15}NO$
m/z-202
202.14362

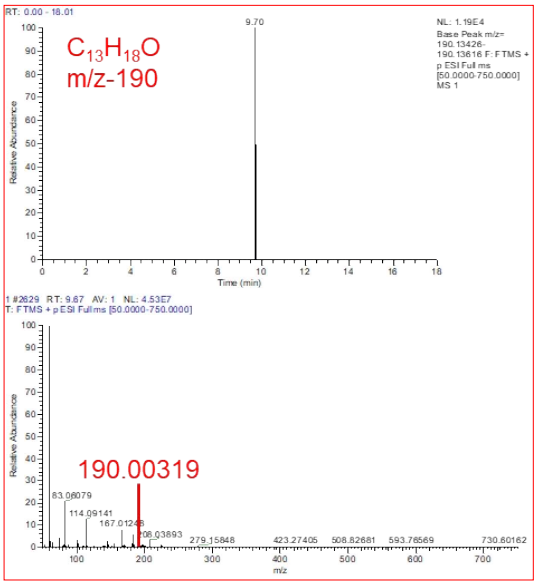
$C_{13}H_{18}O$
m/z-190
190.00319

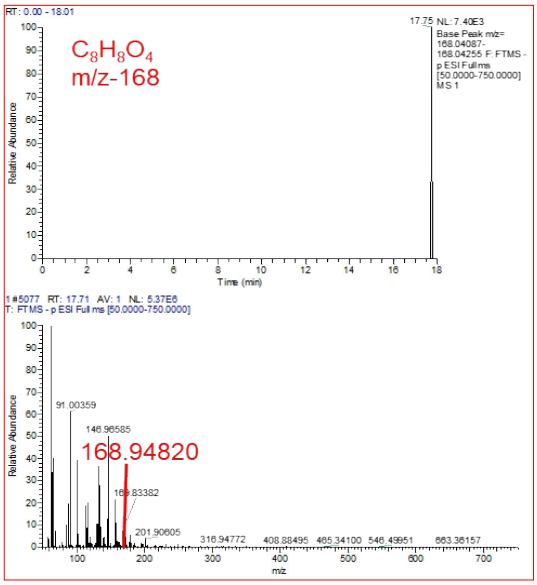
$C_8H_8O_4$
m/z-168
168.94820

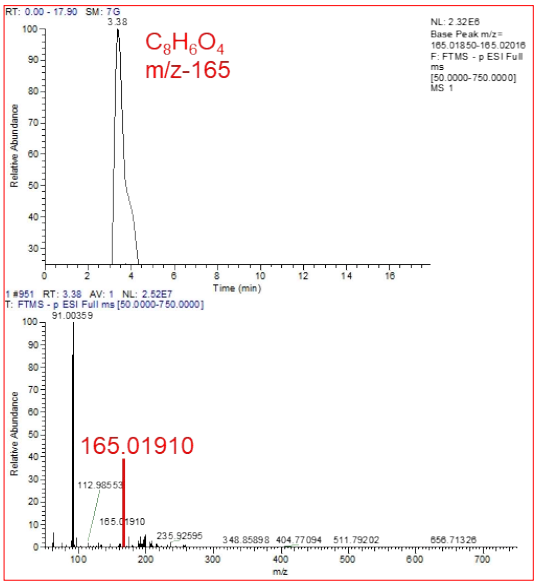
$C_8H_6O_4$
m/z-165
165.01910

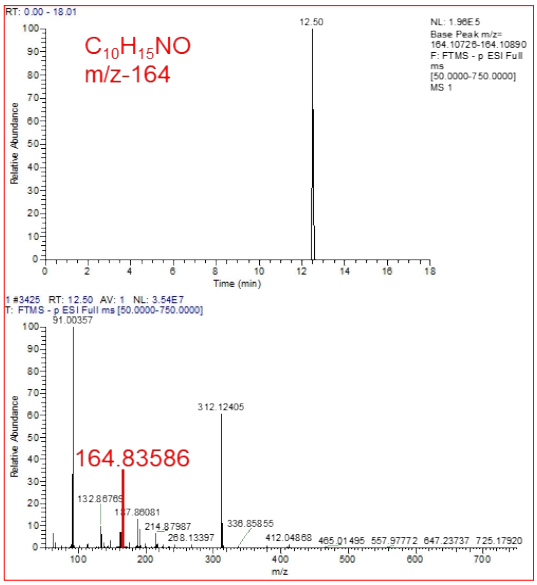
$C_{10}H_{15}NO$
m/z-164
164.83586

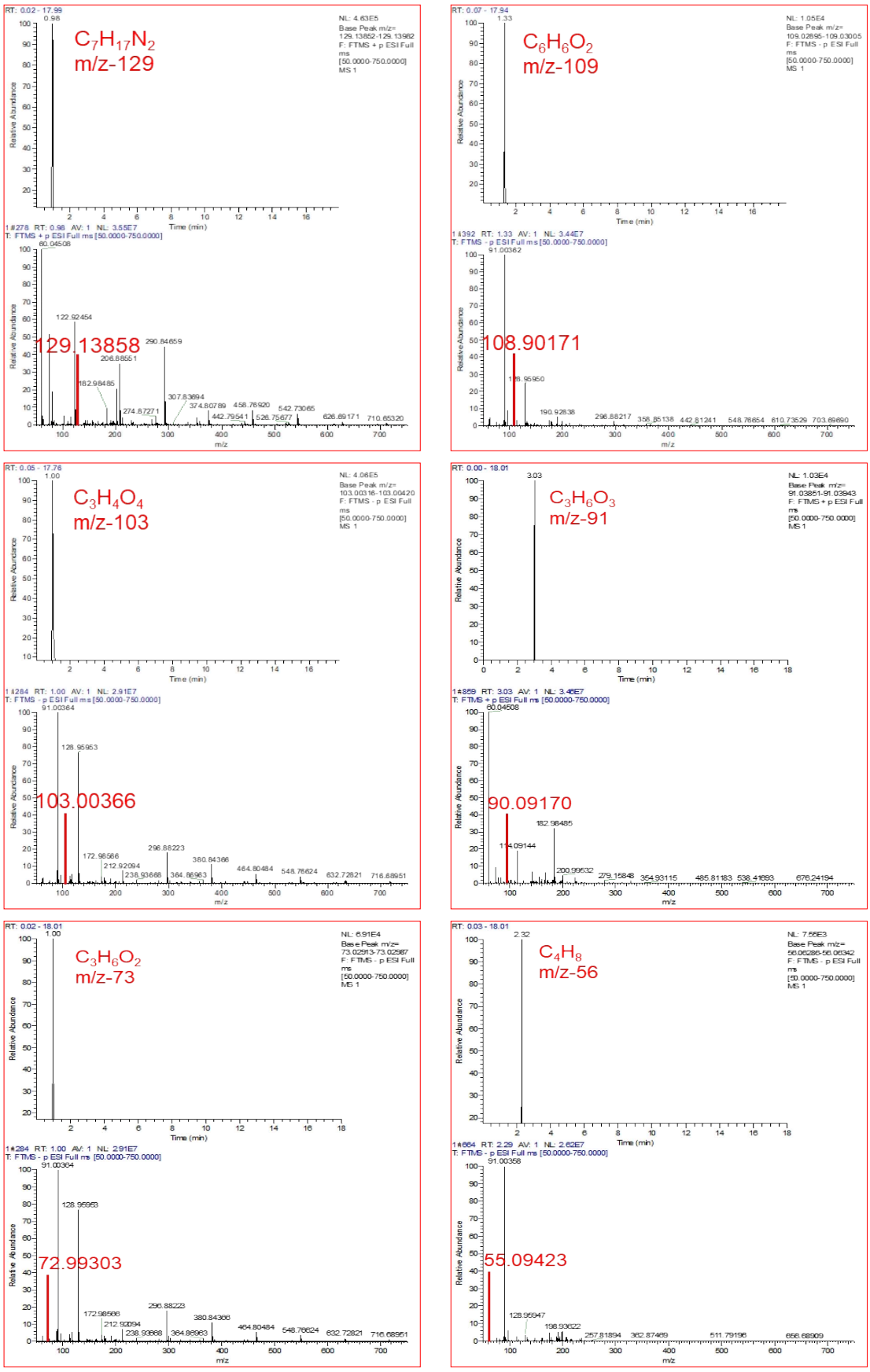

Figure S14 TIC and MS figure of the intermediates formed during degradation of RhB.

3. Tables

Table S1: The mass percentage of Mn metal tested in ICP.

	w_{Mn}
Mn-PDA/CNTs-1	0.42%
Mn-PDA/CNTs-2	4.04%
Mn-PDA/CNTs-3	40.63%

Table S2: Previous studies on H_2O_2 production in MES.

System	Applied Voltage	Catholyte	Current Density	Reactor Volume	Cumulative H_2O_2 Yields	References
CEM-MEC	1.0-1.6 V	Tap water	0.96 A/m^2	110 L (10 L of cathode)	98.48 ± 1.6 mg L^{-1} (15 d)	[1]
MES	0.1-0.8 V	50 mM Na_2SO_4	1.63-3.44 A m^{-2}	20 L (10 L of cathode)	125.36-454.44 mg L^{-1} (42 h)	[2]
MEC	0.3 V	Na_2SO_4	0.6 mA cm^{-2}	315 mL (135 mL of cathode)	39.4 mg L^{-1} h^{-1}	[3]
MEC	0.6 V	50 mM NaCl	0.61 mA cm^{-2}	42 mL (14 mL of cathode)	3.3 mg L^{-1} h^{-1}	[4]
MEC		50 mM Na_2SO_4	0.3 mA cm^{-2}	250 mL	10.8 mg L^{-1} h^{-1}	[5]
MEC	0.8 V	0.1M KOH	15.01-17.50 A/m^2	300 mL (150 mL of cathode)	325.18 mg/L (24 h)	this work

Table S3: Previous studies on RhB degradation in MES.

Cathode	Cathodic pH	Initial RhB concentration	Time (h)	RhB degradation	References
$Fe@Fe_2O_3$/ACF	0.1 mol/L NaCl	10 mg/L	24 h	95.0 ± 3.5 %	[6]
EPE	pH=3	10 mg/L	180 min	91.68 %	[7]
$Fe@Fe_2O_3$/carbon felt	pH≈3	15 mg/L	12 h	95 %	[8]
Mn-PDA/CNT-2/ADFE	pH≈11	6.5 mol/L	8 h	91.79 %	this work

Table S4: An intermediate formed during the degradation of RhB

m/z	分子式	结构式
m/z-443	$C_{28}H_{31}N_2O_3$	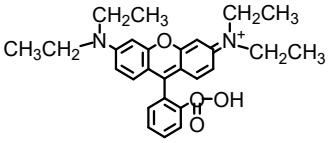
m/z-415	$C_{26}H_{27}N_2O_3$	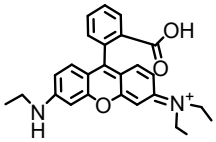
m/z-387	$C_{24}H_{23}N_2O_3$	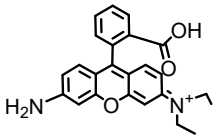
m/z-359	$C_{22}H_{18}N_2O_3$	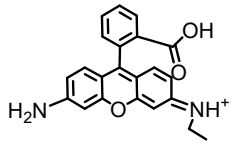
m/z-331	$C_{20}H_{15}N_2O_3$	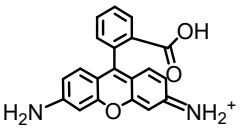
m/z-314	$C_{20}H_{13}NO_3$	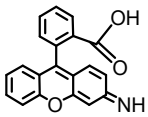
m/z-278	$C_{16}H_{22}O_4$	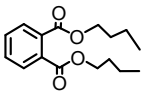
m/z-202	$C_{13}H_{15}NO$	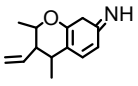
m/z-190	$C_{13}H_{18}O$	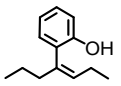
m/z-168	$C_8H_8O_4$	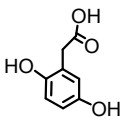

m/z-165	$C_8H_6O_4$	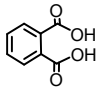
m/z-164	$C_{10}H_{15}NO$	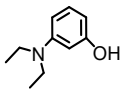
m/z-129	$C_7H_{17}N_2$	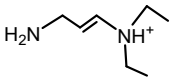
m/z-109	$C_6H_6O_2$	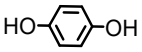
m/z-103	$C_3H_4O_4$	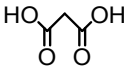
m/z-91	$C_3H_6O_3$	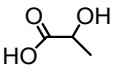
m/z-73	$C_3H_6O_2$	
m/z-56	C_4H_8	

References

[1] SIM J, REID R, HUSSAIN A, et al. Hydrogen peroxide production in a pilot-scale microbial electrolysis cell [J]. Biotechnology Reports, 2018, **19**: e00276.

[2] ZOU R, HASANZADEH A, KHATAEE A, et al. Scaling-up of microbial electrosynthesis with multiple electrodes for in situ production of hydrogen peroxide [J]. iScience, 2021, **24(2)**: 102094.

[3] WANG G, YAO Y, TANG K, et al. Cost-efficient microbial electrosynthesis of hydrogen peroxide on a facile-prepared floating electrode by entrapping oxygen [J]. Bioresource Technology, 2021, **342**: 125995.

[4] LI N, AN J, ZHOU L, et al. A novel carbon black graphite hybrid air-cathode for efficient hydrogen peroxide production in bioelectrochemical systems [J]. Journal of Power Sources, 2016, **306**: 495-502.

[5] ZHANG Q, ZHOU M, REN G, et al. Highly efficient electrosynthesis of hydrogen peroxide on a superhydrophobic three-phase interface by natural air diffusion [J]. nature communications, 2020, **11(1)**: 1731.

[6] P. Xu, D. Zheng, Z. Xie, J. Ma, J. Yu and B. Hou, Separation and Purification Technology, 2020, **234**.

[7] Y. Feng, Z. Zhang, Y. Zhao, L. Song, X. Wang, S. Yang, Y. Long, C. Zhao and L. Qiu, Bioresource Technology, 2019, **283**, 1-9.

[8] L. Zhuang, S. Zhou, Y. Yuan, M. Liu and Y. Wang, Chemical Engineering Journal, 2010, **163**, 160-163.